Journal Pre-proof

Supracellular Measurement of Spatially Varying Mechanical Heterogeneities in Live Monolayers

Alexandra Bermudez, Zachary Gonzalez, Bao Zhao, Ethan Salter, Xuanqing Liu, Leixin Ma, Mohammad Khalid Jawed, Cho-Jui Hsieh, Neil Y.C. Lin

PII: S0006-3495(22)00684-1

DOI: https://doi.org/10.1016/j.bpj.2022.08.024

Reference: BPJ 11920

To appear in: Biophysical Journal

Received Date: 2 April 2022

Accepted Date: 19 August 2022

Please cite this article as: Bermudez A, Gonzalez Z, Zhao B, Salter E, Liu X, Ma L, Jawed MK, Hsieh C-J, Lin NYC, Supracellular Measurement of Spatially Varying Mechanical Heterogeneities in Live Monolayers, *Biophysical Journal* (2022), doi: https://doi.org/10.1016/j.bpj.2022.08.024.

This is a PDF file of an article that has undergone enhancements after acceptance, such as the addition of a cover page and metadata, and formatting for readability, but it is not yet the definitive version of record. This version will undergo additional copyediting, typesetting and review before it is published in its final form, but we are providing this version to give early visibility of the article. Please note that, during the production process, errors may be discovered which could affect the content, and all legal disclaimers that apply to the journal pertain.

© 2022 Biophysical Society.



Manuscript submitted to **Biophysical** Journal **Article**

Supracellular Measurement of Spatially Varying **Mechanical Heterogeneities in Live Monolayers**

Alexandra Bermudez^{1,2*}, Zachary Gonzalez^{1,3}, Bao Zhao¹, Ethan Salter^{1,2}, Xuanqing Liu⁴, Leixin Ma¹, Mohammad Khalid Jawed¹, Cho-Jui Hsieh⁴, and Neil Y.C. Lin^{1,2,5*}

ABSTRACT The mechanical properties of tissues have profound impacts on a wide range of biological processes such as embryo development (1, 2), wound healing (3-6), and disease progression (7). Specifically, the spatially varying moduli of cells largely influence the local tissue deformation and intercellular interaction. Despite the importance of characterizing such a heterogeneous mechanical property, it has remained difficult to measure the supracellular modulus field in live cell layers with a high-throughput and minimal perturbation. In this work, we developed a monolayer effective modulus measurement by integrating a custom cell stretcher, light microscopy, and Al-based inference. Our approach first quantifies the heterogeneous deformation of a slightly stretched cell layer, and converts the measured strain fields into an effective modulus field using an AI inference. This method allowed us to directly visualize the effective modulus distribution of thousands of cells virtually instantly. We characterized the mean value, standard deviation, and correlation length of the effective cell modulus for epithelial cells and fibroblasts, which are in agreement with previous results. We also observed a mild correlation between cell area and stiffness in jammed epithelia, suggesting the influence of cell modulus on packing. Overall, our reported experimental platform provides a valuable alternative cell mechanics measurement tool that can be integrated with microscopy-based characterizations.

Investigating tissue stiffness is critical for understanding fundamental cell behavior such as cell SIGNIFICANCE migration, development, and division (8). While many useful tools for characterizing tissue stiffness have recently been developed, it remains challenging to measure the supracellular modulus field of live cell layers with a high-throughput and minimal perturbation. In this work, we integrated a custom cell stretcher, light microscopy, and an Al-based inference model to characterize a tissue's supracellular modulus distribution by slightly deforming a cell layer cultured on an ultra-thin and ultra-soft polymer membrane. In addition to measuring the mean effective modulus and modulus fluctuation for both epithelial cell and fibroblast layers, we identified a modulus correlation length spanning a few cells, and a mild correlation between cell area and stiffness.

INTRODUCTION

The mechanical properties of tissues play an essential role in regulating various biological processes and can be used as a biomarker for label-free, low cost, and rapid disease diagnosis (1, 9-15). During embryogenesis, tissue viscoelasticity instructs the differentiation, migration, and organization of cells (12–15). In developed organs, tissue stiffness regulates the cellular homeostasis and physiological functions (1, 9). In diseased organs, tissue modulus has been shown to act as a physical cue influencing the pathogenesis and progression of fibrosis (9), asthma (16), and Crohn's disease (17). Moreover, the tumoral tissue elasticity has been found to correlate with malignancy, metastatic potential, and drug resistance (10, 18).

To study these mechanically regulated processes, the ability to characterize cell modulus heterogeneities at the supracellular scale is critical. For example, cell migration is largely impacted by local cell stiffness, which determines the system's response to the intercellular force (19–21). This cell modulus variation has also been shown to induce cell competition that functions as a quality control mechanism by expelling "loser cells" (22, 23). Recently, it has been demonstrated that this modulus-regulated cell competition

¹Department of Mechanical and Aerospace Engineering, University of California, Los Angeles, California 90095, USA

²Department of Bioengineering, University of California, Los Angeles, California 90095, USA

³Department of Physics and Astronomy, University of California, Los Angeles, California 90095, USA

⁴Department of Computer Science, University of California, Los Angeles, California 90095, USA

⁵Institute for Quantitative and Computational Biosciences, University of California, Los Angeles, 90095, USA

^{*}Correspondence: abermudez22@g.ucla.edu, neillin@g.ucla.edu

can be harnessed as a defense against precancerous cells (24, 25).

While many pioneering cell stiffness measurement methods have been developed in the past few decades, characterizing the supracellular spatial distribution of cell modulus remains challenging. One of the earliest methods for measuring cell modulus is micropipette aspiration, a cost-effective technique that can track a sample's mechanical properties over time in vivo (26, 27). Although micropipette aspiration can achieve a cell-level resolution, it does so in a low-throughput manner and requires cell detachment for characterizing adherent cells (26, 28). Atomic force microscopy (AFM) is currently the most widely used tool for studying adherent cell stiffness at a subcellular resolution. When using a pyramidal tip, the measured modulus, however, may correspond to a specific organelle which does not represent the overall cell stiffness, introducing uncertainties in interpreting the supracellular measurement (29–31). Moreover, depending on the indentation used or region probed, it can be difficult to distinguish the cellular contributions to the measurement from that of the substrate for penetration depths greater than 10% of the cell thickness (18). Lastly, AFM cannot directly probe the in-plane modulus of the monolayer, which is more relevant to physiological processes compared to the transverse modulus typically acquired by AFM.

Another common technique is magnetic twisting cytometry (MTC), which is a high-throughput method able to characterize hundreds of cells by twisting magnetic microbeads that bind to membrane receptors (32). The binding of the microbead to the cell surface, however, can induce formation of focal adhesion complex, which reorganizes the cytoskeleton and can alter cells' rheological properties. Additionally, the substrate can interfere with the MTC measurement, akin to AFM (32). Similar to the working mechanism of MTC, a recent experiment used magnetic droplets to probe the local tissue stiffness. While this method addresses the cytoskeletal reorganization and substrate issues, it can be difficult to generate cell-scale ferrofluid droplets, which determine the spatial resolution of the measurement (33). Cell shape based inference models are a non-perturbative approach for extracting a monolayer's mechanical property at the cellular or tissue level using microscopy (34). In this method, only stress is directly determined, thus requiring independent local strain measurements to infer the modulus (35–37), in which this approach, however, has remained untested. Alternatively, cell stretchers are a versatile device that have been routinely used to characterize in vitro cell monolayer mechanics. It has been demonstrated that by either culturing cell layers on thin elastomer substrates, or by detaching intact cell layers from the substrates, the overall monolayer stiffness can be determined using a stretcher (11). Building upon these studies, we developed a monolayer mechanics measurement platform by integrating a custom-built stretcher, transmitted light microscopy, and AI inference. This integration allows us to directly visualize the heterogeneous effective modulus field

in live cell monolayers. Additionally, we unmask the mechanical contributions of cells from the substrate by growing the cells on a soft (12.7 kPa) and thin (18.9 μm) biocompatible membrane (Figs. 1A and B). Our stretcher features an imaging window that enables us to conduct high-magnification transmitted light microscopy during experiments, which resolves the supracellular variation of cell deformation due to the applied strain. The AI inference model then converts the measured deformation field into an effective modulus field (Fig. 1C). Using this measurement platform, we characterized the effective modulus distribution in live epithelial (Fig. 1D) and fibroblast cell layers. These results allowed us to identify a mild correlation between cell moduli and morphological features in jammed Madin-Darby canine kidney (MDCK)

MATERIALS AND METHODS

Cell culture

MDCK cells were cultured in 1X Dulbecco's Modified Eagle media (Gibco, 11885084) supplemented with 5% fetal bovine serum (FBS) (Gibco, 16000044) and 1% penicillinstreptomycin (P/S) (Gibco, 15140122), where media was changed every 2 days. During weekly subculturing, ~80% confluent cells were passaged using 0.05% trypsin-EDTA (Gibco, 25300054). 3T3 cells were cultured using the same base media but supplemented with 10% FBS and 1% P/S with all other conditions identical to that of the MDCK cells. MDCK and 3T3 cells were seeded using a density of 10,000 cells/cm².

PDMS membrane fabrication

To fabricate the polydimethylsiloxane (PDMS) membrane, we spin coated Sylgard 184 (base-curing agent ratio = 50:1) at a 2,000 RPM speed for 5 minutes on a glass coverslip that was previously coated with 10% (m/v%) polyvinyl alcohol (PVA) at a speed of 1,000 RPM for 2 minutes. We found that using concentrated 10% PVA for coating the sacrificial layer ensures membrane thickness uniformity. After attaching a cell stretcher jig to the PDMS surface, the composite was then cured at 150°C for 35 minutes. The PDMS-jig setup was autoclaved, treated with 25 µg/ml fibronectin (R&D Systems, 1030FN05M), and incubated at 37°C for 30 minutes. The sample was then washed with phosphate-buffered saline twice before seeding cells at a 10,000 cells/cm² density. During culture, the media dissolved the water-soluble PVA layer, lifting-off the PDMS from the coverslip.

To measure the stiffness of the PDMS, we fabricated and clamped 70 mm \times 18 mm \times 2 mm PDMS strips to an Instron 5944 and stretched it at a rate of 10 mm/min. The acquired stress-strain curves were used to calculate the Young's modulus by analyzing their slopes in the linear regime (Fig. S1A). PDMS membrane thickness was characterized by optically imaging (40X objective) the cross-section of a

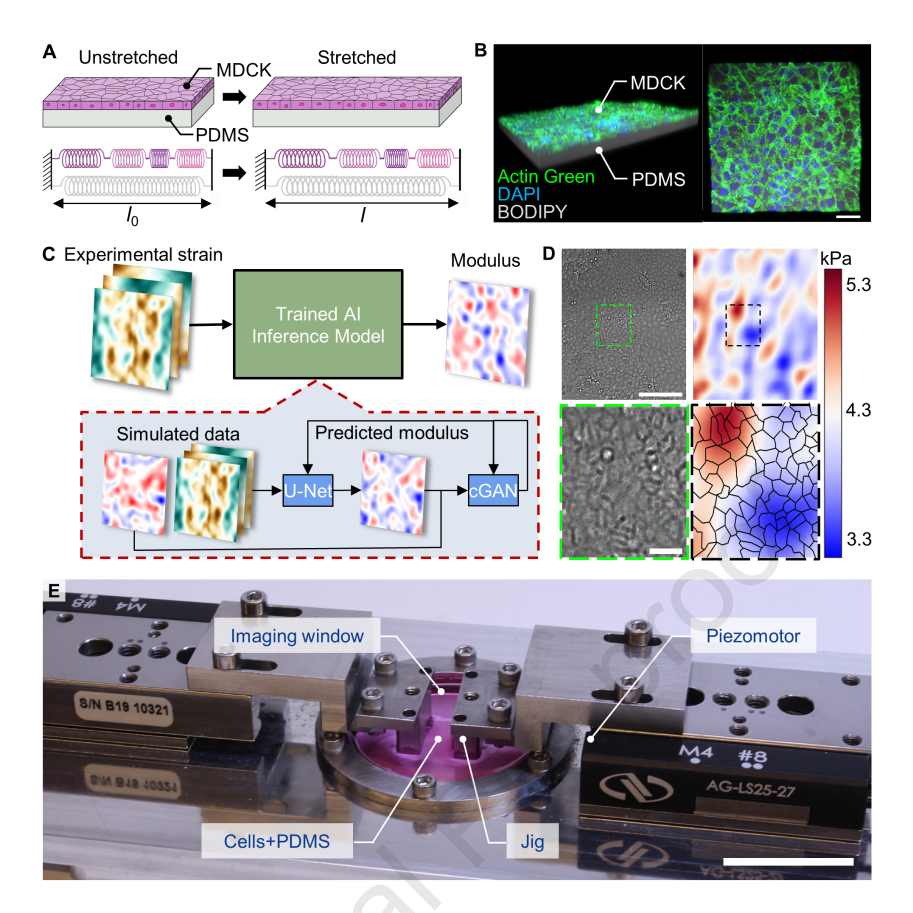


Figure 1: Visualization of mechanical heterogeneities in cell monolayers (A) By growing a cell monolayer (MDCK) on a ultrasoft PDMS membrane, the cell mechanical heterogeneity, which is illustrated by distinct Hookean springs, can be revealed by stretching the bilayer system. (B) 3D reconstruction of a cell-PDMS bilayer tested in our experiment. (C) An AI inference model is used to convert experimentally measured strain fields into effective modulus distributions, in which the inference model (cGAN U-Net) is trained using finite element analysis data. (D) Example DIC (left) and effective modulus (right) data of MDCK cells. Dashed box indicates the zoom-in area. (E) Our cell stretcher applies a uniform tensile strain to a free-standing cell-PDMS bilayer suspended by the jig legs, using piezomotors. The imaging window allows for microscopy while containing the media during experiments. For B, scale bar = $50 \mu m$. For D, scale bars = $200 \mu m$ and $50 \mu m$ for top and bottom images, respectively. For E, scale bar = 2.5 cm.

PDMS layer on the coverslip (Fig. S1B) and measuring its thickness using ImageJ (Figs. S1C-E).

Cell stretching data acquisition and analysis

To prepare the cell-PDMS bilayer sample for stretching (Fig. S1F), the bilayer spanning the two jig legs was cut and then mounted to the cell stretcher as shown in Fig. S1G and S2A. Subsequently, media was added to the media chamber to submerge the sample, and the supportive T-bar was removed. The stretcher assembly (Fig. S2B) was placed on a microscope (Nikon Ti) and stretched the sample at a rate of 25 µm/sec until 5% strain (0.5% strain/sec), corresponding to a 250 μm stretch for a duration of 10 seconds. Simultaneously, differential interference contrast (DIC) images were acquired using a 10X objective (NA 0.45) at 20 fps. The acquired images were

registered using the ImageJ plugin StackReg (38), and used for particle image velocimetry (PIV) analysis with PIVlab (39) to determine the displacement of cells between the initial unstretched image and the final stretched image. Strain-xx $(\epsilon_{xx} = \Delta u_x/\Delta x)$, strain-xy $(\epsilon_{xy} = 0.5(\Delta u_y/\Delta y + \Delta v_x/\Delta x))$, and strain-yy ($\epsilon_{yy} = \Delta v_y/\Delta y$) values were calculated and assigned to points in the image using MATLAB, where Δu_x is x-displacement difference of x-adjacent elements, Δu_{y} is x-displacement difference of y-adjacent elements, Δv_x is y-displacement difference of x-adjacent elements, Δv_y is y-displacement difference of y-adjacent elements, Δx is xposition difference of adjacent elements, and Δy is y-position difference of adjacent elements.

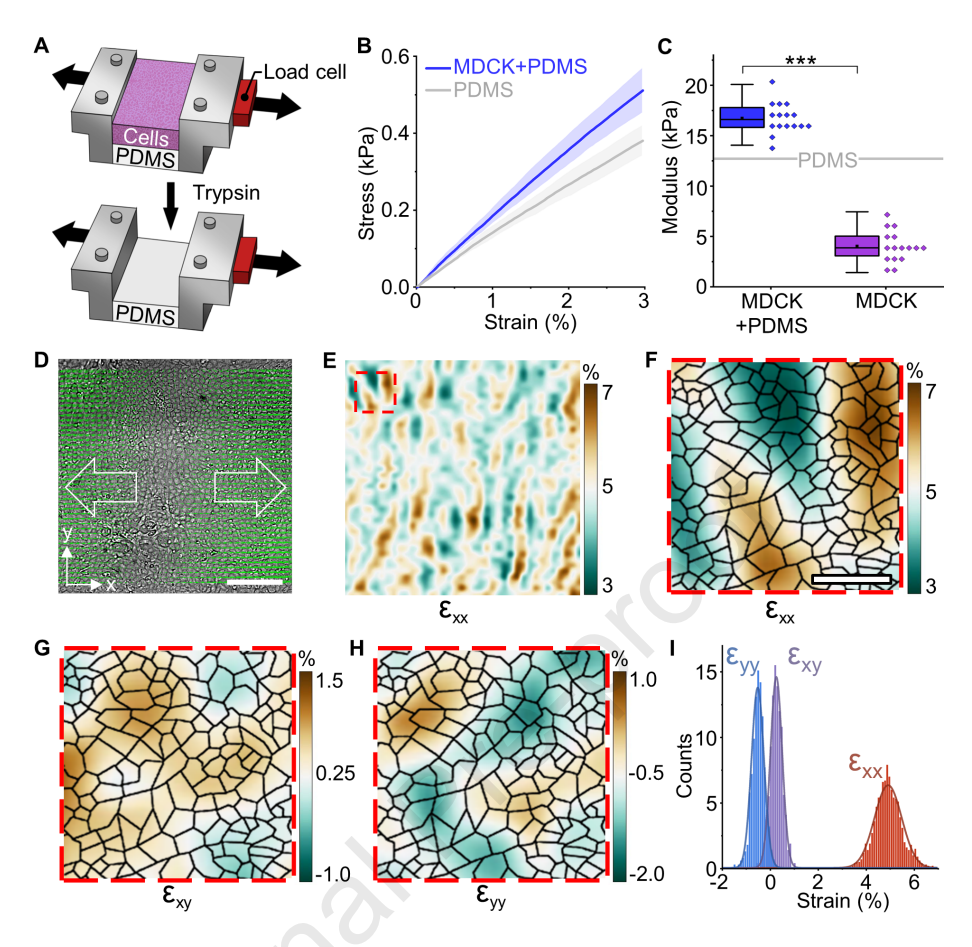


Figure 2: Heterogeneous strain responses in MDCK monolayers (A) After measuring the effective modulus of the cell-PDMS sample, we used trypsin to detach the cells and measured the cell-free PDMS membrane modulus. (B) Stress-strain curves for cell-PDMS (MDCK+PDMS) and PDMS samples. Shaded area denotes the standard deviation. (C) Using the Hookean model illustrated in Fig. 1A, MDCK stiffness (4.0 ± 1.5 kPa) was estimated using equation (1). n = 16. (D) DIC image of a stretched MDCK sample annotated with displacement fields. (E) Heatmap of the xx component (ϵ_{xx}) of strain calculated from the displacement field in (D). (E-H) Close up of (E) showing heatmaps of ϵ_{xx} , ϵ_{xy} , and ϵ_{yy} , respectively. (I) Histograms for all strain components fitted by Gaussian curves. Scale bar for D-E = 200 μm. Scale bar for F-H = 50 μm.

Cell-PDMS bilayer mechanical measurement

To measure the overall sample stiffness, the cell-PDMS bilayer was cyclically stretched to 5% strain using the cell stretcher while force was recorded by a force transducer (FUTEK LSB201 LSB205 Load Cell). Following this, the media in the chamber was replaced with 0.5% trypsin-EDTA and the sample was incubated at 37 °C for cell detachment (Fig. 2A). After confirming cell detachment using light microscopy, the cell-free PDMS membrane was then again cyclically stretched to 5% strain while force was measured.

Al inference model training

To generate the datasets for training the strain-to-modulus AI inference, we performed a series of finite element analyses (FEA) that described the mechanical response of cell-PDMS bilayers under tensile strain. The PDMS and cell layers were

individually modeled in 3D using triangular shell elements in Abaqus, in which the model parameters including cell mean modulus (4.0 kPa for MDCK and 12.2 kPa for 3T3 cells), cell height (9.2 μ m for MDCK and 6.3 μ m for 3T3 cells (40)), Poisson ratio (0.5 for both MDCK and 3T3 cells (41), PDMS modulus (12.7 kPa), and PDMS thickness (18.9 μ m), were either taken from previous studies or determined experimentally (Fig. S1). We discretize the finite element to 16,638 three-node elements, in which the size of the FE mesh is controlled to be \sim 8.3 μ m. This fine mesh setting allows us to vary the length scale of heterogeneities in FEA simulations on supracellular scales, in which all data were included for AI model training.

The cell layer and PDMS membrane were modeled as incompressible elastic materials. We impose material continuity in simulations, suggesting that the cell layer mechanically interacts with its surroundings, where the interpretation of

such continuity may have different implications depending on the size of the cell. Specifically, for small (10-15 μ m) MDCK cells, this continuity implies that cells are directly interacting with neighboring cells, whereas in larger ($\sim 50 \mu m$) 3T3 cells, this continuity implies continuity of cellular components within a cell.

To simulate cell modulus heterogeneity, we generated random cell modulus fields from normal or log-normal distribution with a standard deviation ranging from 30% to 70% of the mean modulus. In simulation, one side of the sample was uniaxially stretched to 5% strain where a non-slip boundary condition was applied at the cell-PDMS interface.

In other cell stretching experiments, cell-substrate adhesions have been observed to remain intact and stable, especially for short time and length scales (43–45). The displacement of individual cells was recorded, and the corresponding strain fields were calculated (Fig. S3A). The resulting strain (ϵ_{xx} , ϵ_{xy} , and ϵ_{yy}) and modulus fields were loaded into the AI model training framework, as summarized in Fig. S3B.

Statistical analysis

Data were reported as mean values \pm standard deviation. Statistical analysis was performed using OriginLab. Statistical significance was determined using paired t-tests. Significance levels are indicated with asterisks in each figure. P-values less than 0.05, 0.01, and 0.001 were denoted by *, **, and ***, respectively.

RESULTS

Visualizing monolayer mechanical heterogeneities

To visualize the spatially varying mechanical properties of cell monolayers, we cultured MDCK cells on a PDMS membrane (Fig. 1B) and imaged its heterogeneous response to a tensile strain. During stretching, the tested cell-PDMS bilayer behaves analogously to a spring system, in which individual cells with different moduli can be considered as springs with different spring constants Fig. 1A). In this approach, it is critical to use a thin, soft, and freestanding PDMS membrane to prevent the substrate from masking the cell contribution to the overall strain response. Stretched elastomeric membranes such as PDMS have been routinely used to demonstrate uniform displacement fields and have been widely used for characterizing cell deformation (46–48).

The freestanding PDMS membrane was fabricated by adapting a previous protocol (49, 50) in which a sacrificial PVA layer was utilized to facilitate the membrane lift-off process, as described in *PDMS Membrane Fabrication*. We then mounted the sample on our custom-made cell stretcher, which features an imaging window that is compatible with inverted microscopy and functions as a cell culture media reservoir (Fig. S2A). The piezomotors of our stretcher provide stretching motion stability to ensure imaging focus during experiments. To prevent folding and tearing of the thin bilayer, the two jig legs that suspend the sample are fixed by a connecting T-bar during handling, which is then removed after sample mounting (Fig. S1G).

To confirm that the mechanical contribution from the cells can be observed in our bilayer system, we used a force transducer to measure the stress response difference between the cell-PDMS bilayer and PDMS-only samples. We first measured the effective modulus of the bilayer and repeated the measurement for the cell-free PDMS membrane by enzymatically detaching the cells (Fig. 2A). This procedure is similar to the cell removal protocol routinely used in traction force microscopy for characterizing the substrate deformation (51, 52). As shown in Fig. 2B, we found that the cell-PDMS bilayer stress-strain curve exhibited a slope greater than that of the cell-free PDMS, which is attributed to the mechanical contribution from the cell layer. Using the spring analogy as depicted in Fig. 1A, we then calculated the cell monolayer modulus (Fig. 2C) E_c :

$$E_c = \frac{E_b(A_m + A_c) - E_m A_m}{A_c} \sim 4.0 \pm 1.5 \text{ kPa}$$
 (1)

Here, $E_b = 16.7 \pm 1.5 \text{ kPa}$, $E_m = 12.7 \pm 4.2 \text{ kPa}$, $A_m = 18.9 \pm 12.7 \pm 1.2 \text{ kPa}$ $0.5 \,\mu\text{m}$, and $A_c = 9.2 \pm 0.7 \,\mu\text{m}$ is the bilayer effective modulus, membrane modulus, membrane cross-sectional area, and cell monolayer cross-sectional area, respectively for MDCK samples. In MDCK FEA simulations, E_c was used as the mean modulus, and A_c was determined using confocal microscopy (Fig. S1F). The remaining parameters were determined as described in AI inference model training. In addition, using a similar measurement approach, MDCK cells treated with 25 µM blebbistatin for 24 hours exhibited a 3-fold lower modulus compared to untreated MDCK cells (Figs. S4A-D). This finding further validates that the PDMS membrane can reveal the mechanical contribution arising from the cell layer.

After validating the mechanical contribution from cells in our bilayer samples, we mounted the stretcher on a microscope and applied a 5% tensile strain to a cell-PDMS sample while simultaneously imaging cell deformation. With the acquired image data, we performed PIV to determine the displacement field (Fig. 2D) resulting from the stretch. Since our applied tensile deformation is symmetric, the displacement field shows minimal x-y translation which maximizes the analyzable field of view.

We then calculated the corresponding strain fields, where the components $(\epsilon_{xx}, \epsilon_{xy}, \text{ and } \epsilon_{yy})$ are shown in Figs. 2E-H. Specifically, we found that ϵ_{xx} has a mean of ~ 4.9%, which was consistent to the applied global strain value. In agreement with previous studies (53, 54), we observed spatial fluctuations in all strain components which suggest the presence of mechanical heterogeneity in the tested MDCK monolayer. For example, ϵ_{xx} had a relative standard deviation of $\sim 20\%$. Additionally, we found that ϵ_{xy} and ϵ_{yy} have mean values and fluctuations an order of magnitude less than that of ϵ_{xx} (Fig. 2I), which was anticipated since the stretch was applied

uniaxially in the x-direction. Importantly, all these values are greater than the strain uncertainty associated with PIV limitations (55). Furthermore, the high image resolution (1 pixel $\sim 0.65 \, \mu m$) of our system allowed us to visualize strain field heterogeneity at the cellular level. As shown in Fig. 2F, we found that the strain fluctuation of ϵ_{xx} spans a few cells. This finding is consistent with the cell mechanical heterogeneity found in AFM measurements (56) and free-standing epithelium stretching experiments (42).

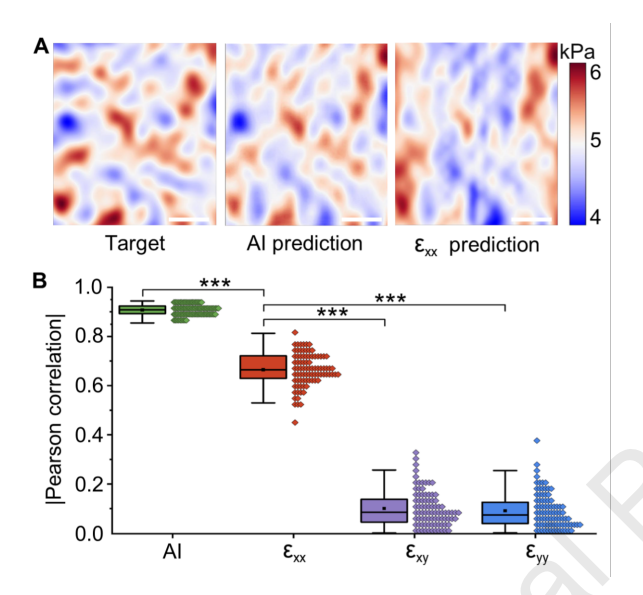


Figure 3: Strain-modulus AI inference (A) Comparison of the modulus fields generated by FEA simulation (Target), predicted by the AI inference model, and predicted from only strain-xx values. (B) Pearson correlation between the target modulus values and predictions made using the AI inference, ϵ_{xx} , ϵ_{xy} , and ϵ_{yy} . We found that ϵ_{xx} exhibits a higher correlation than xy and yy components, and AI-predicted values are significantly more correlated than ϵ_{xx} . Scale bars for A = 200 μ m.

Converting strain responses to modulus fields

The strain field of a deformed material is directly determined by the moduli of its constituents and the globally applied strain. Conversely, having access to the strain components of cells within a stretched cell monolayer allows us to infer the effective modulus field from the strain fields. However, converting strain fields into a modulus distribution can be challenging due to their complex relationship in structurally disordered and mechanically heterogeneous systems. In our approach, the deformation of a cell is influenced by both its own stiffness and the surrounding modulus field. Thus, the determination of local effective modulus values requires the knowledge of the entire strain fields for all components, rather than just the value at a local position. To capture such a high-

dimensional strain-modulus relationship, we employed a U-net based neural network architecture that analyzes both strain and modulus fields across multiple length scales. Specifically, our AI model utilized a generator and a discriminator, which are both convolutional neural networks (Fig. 1C). The generator network was based on a U-Net architecture (59, 60) and learned the nonlinear relationship between the FEA simulated ϵ_{xx} , ϵ_{xy} , and ϵ_{yy} distributions and its corresponding FEA simulated modulus distribution. During the training process, the neural network minimizes the loss function by calculating the pixel-to-pixel differences between the prediction and target. Here, the target is the FEA simulated modulus distribution of a cell layer. Our three strain inputs first propagated through the U-Net, where the resulting generator output (predicted modulus) was loaded into the discriminator network. The discriminator network then used a conditional generative adversarial network (cGAN) (61) to estimate the probability of similarity between the predicted and target image. The discriminator output, which is an adaptive loss function, is iterated over a set number of cycles through the model to optimize the prediction. Once this iteration process is completed, the resulting trained model was used for predicting effective modulus distributions of cell layers from experimental ϵ_{xx} , ϵ_{xy} , and ϵ_{yy} distributions. Similar methods have been commonly utilized in a wide range of 2D field conversion tasks including the translation, segmentation, and classification of image data (62–64).

To train our AI model, we used FEA to numerically model a stretched bilayer system that closely recapitulates the heterogeneous modulus distribution in the cell monolayer. Specifically, since our experiment operates on the time scale of seconds, we model our cell and PDMS layer individually as elastic materials (65–67). Here, we assume a non-slip boundary condition between the cell and PDMS layers such that the applied strain results in a direct mechanical deformation of cell layer (Figs. S5A-C). This training framework is synthetic data-based, which has been commonly used in vision research, and shown to yield robust and traceable AI prediction performance (68, 69). More importantly, the use of FEA data grants us access to the strain inputs ϵ_{xx} , ϵ_{xy} , and ϵ_{yy} and the corresponding modulus outputs (i.e., ground truth), which is infeasible to obtain experimentally. The AI model was trained by utilizing the generated FEA data to infer the general strain-modulus relationship, which was used to construct a conversion function capable of determining the effective modulus field from experimental strain fields.

To characterize the AI prediction accuracy, we compared the ground truth (i.e., modulus distribution assigned in FEA) to the AI predicted effective modulus field (Fig. 3A and Fig. S6A). Additionally, to test whether a single-component strain measurement would be sufficient for inferring the effective modulus field, we included an ϵ_{xx} predicted modulus distribution, which was obtained by using the best fit between FEA simulated ϵ_{xx} and modulus values (Fig. S6B). We found that while the effective modulus field can be roughly estimated using solely the tensile strain component, ϵ_{xx} , the most ac-

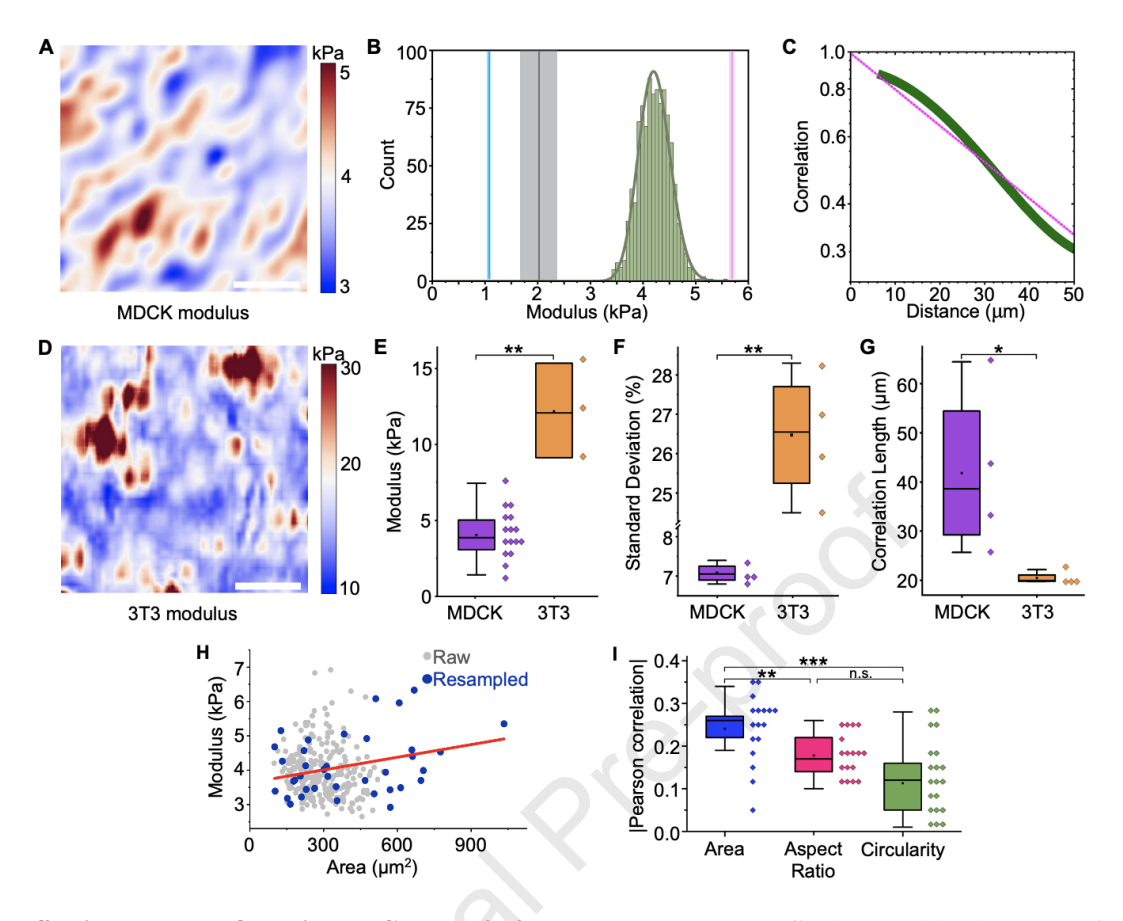


Figure 4: Effective modulus fields in MDCK and 3T3 cell monolayers (A) Effective modulus heatmap of an MDCK monolayer predicted by AI inference. (B) Histogram of (A) showing the AI-predicted MDCK effective modulus in comparison to literature values. The cyan, gray, and pink lines denote the mean moduli reported in (56–58), respectively, with the standard deviation illustrated by the shaded area. (C) Correlation function of the measured MDCK effective modulus field exhibits an exponential decay $\sim e^{-d/45.2}$ (dashed magenta line). (D) Effective modulus heatmap of a 3T3 cell layer predicted by the AI inference. (E) Mean moduli for MDCK and 3T3 cells determined using the force measurement. The 3T3 cells are approximately four times stiffer than MDCK cells. (F) 3T3 cells exhibit a greater effective modulus fluctuation (standard deviation ~ 27%) than that of MDCK cells (standard deviation $\sim 7\%$). (G) MDCK cells exhibited an effective modulus distribution that is more spatially correlated (correlation length $\sim 40~\mu m$) than that of 3T3 cells (correlation length $\sim 20~\mu m$). (H) Effective modulus and area measurements for individual cells (n = 286). Blue points denote a resampled dataset (n = 36) that has an even probability distribution across area values. The fit for resampled data (red line) shows a correlation between effective cell modulus and area. (I) Pearson correlation between morphological features and effective modulus values. We observed weak correlation between effective cell modulus, area, and aspect ratio. Scale bar for A and D = 200 μ m.

curate effective modulus field is inferred by considering the spatial distribution of all three strain components. As shown in Fig. 3A, the AI prediction captures both the localization and fluctuation level of the modulus ground truth significantly better than the ϵ_{xx} prediction, suggesting that some mechanical heterogeneities are only reflected in the spatial distribution of ϵ_{xy} and ϵ_{yy} .

To quantify the accuracy of different effective modulus prediction methods, we calculated the Pearson correlation coefficient between ground truth modulus values and the values predicted using the AI, ϵ_{xx} , ϵ_{xy} , and ϵ_{yy} inferences. Our results, shown in Fig. 3B, suggest that the strain components

 ϵ_{xy} , and ϵ_{yy} alone do not provide adequate information for predicting modulus. Furthermore, we found that the AI prediction accuracy (correlation ~ 0.91) is significantly higher than that achieved by ϵ_{xx} prediction (correlation ~ 0.66). This finding confirms our hypothesis that the spatial distribution of all strain components are required to accurately predict the effective modulus field. We also found that the high accuracy of AI prediction can be achieved by training the model within 400 FEA data sets (Fig. S6C). Lastly, compared to conventional reverse problem approaches (70–72), our AI-based forward method enables us to overcome technical solution limitations such as existence, uniqueness, and continuity, which are requirements for solution stability (73).

Spatial distributions of cell moduli

We applied our AI model to convert the MDCK strain data into an effective modulus field (Figs. 4A and S7A). The resulting MDCK effective modulus was 4.0 kPa \pm 1.5 kPa (~38% fluctuation), in which its probability distribution can be approximated by a Gaussian function (Fig. 4B). Compared to literature values obtained from AFM, our measured mean effective modulus is of the same order of magnitude (Fig. 4B), in which the differences may be attributed to different levels of jamming and substrates used (56-58). The similarity between our modulus and AFM measurement may suggest that the in-plane elastic modulus (stretching) is comparable to the transverse elastic modulus (AFM) in MDCK cells, implying that the cellular and organelle structural anisotropies do not necessarily lead to cell modulus anisotropy. We also characterized the length scale of the effective modulus fluctuation by calculating the spatial autocorrelation function:

$$C(\vec{d}) = \frac{\langle (E(\vec{x} + \vec{d}) - \bar{E})(E(\vec{x}) - \bar{E})\rangle_{\vec{x}}}{E_{var}}$$
 (2)

Here, $E(\vec{x})$ is the effective modulus value at position \vec{x} , whereas \bar{E} and E_{var} are the mean and variance of the effective modulus, respectively. For simplicity, we plot the radial part of the correlation function (i.e., using the magnitude of \vec{d} as the variable) in Fig. 4C. As shown, we observed an exponential decay $\sim e^{-d/45.2\mu m}$, suggesting a correlation length of $45.2\mu m \sim 3$ cells. Our measurement is consistent with the intercellular modulus correlation determined using AFM, confirming the spontaneous modulus correlation in jammed epithelial monolayers (56).

To demonstrate that our approach is compatible with other adherent cell types, we implemented the same experimental approach to characterize 3T3 fibroblast cell layers (Figs. 4D and S7B). Consistent with previous studies (56–58, 74–77), we found that 3T3 cells exhibited a higher mean effective modulus (12.2 kPa) compared to MDCK cells (4.0 kPa) (Fig. 4E) . Moreover, we observed that the 3T3 culture shows a greater effective modulus fluctuation than that of MDCK (Fig. 4F). The large effective modulus fluctuation may be related to the differences in underlying cytoskeletal activity observed in 3T3 cells (78) We also found the correlation length of 3T3 cell effective modulus is approximately half that of MDCK cell effective modulus (Fig. 4G). As suggested by previous studies, the relatively long correlation length of MDCK effective modulus might be associated with their intercellular adhesions (56). We acknowledge that unlike MDCK monolayers, there are no intercellular junctions present in 3T3 monolayers, and thus the lack of such junctions may not be captured in the continuity assumption imposed in our FEA simulations. Nevertheless, the space between cell boundaries only occupied roughly 5% of the analyzable field of view (Figs. S7A and S7B), suggesting that a majority of the heterogeneity observed

is within the cell, and can therefore be interpreted as cellular mechanical heterogeneity.

Since our effective modulus measurement is microscopybased, we can additionally evaluate the morphological phenotype of cells under tensile strain. This capability enabled us to investigate the relationship between effective modulus and morphology in MDCK cells. We analyzed and plotted cell moduli as a function of four morphological features: cell area (Figs. 4H and S8A), aspect ratio (Figs. S8B and S8C), circularity (Figs. S8D and S8E), and shape index (Figs. S8F and S8G). Overall, the distribution of raw data did not show a visually obvious correlation between cell effective modulus and area. The difficulty to visualize such a correlation is associated with the relatively narrow distribution of cell size, in which most data points are between the area of 200 μm^2 and 400 μm^2 . To balance the contributions from the data points outside this range, we resampled the data such that cells across the range of area are randomly selected with equal probability. Specifically, we resampled the data so that there was an equal number of cells in bins of 50 μ m². The resampled dataset then revealed a mild effective modulus-area correlation that was previously masked (Fig. S8A). Using the same data sampling approach, we also analyzed the cell aspect ratio, circularity, and shape index, in which we did not observe a strong correlation with cell effective modulus (Fig. 4I).

Our modulus-area result suggests that the cell modulus may play a role in determining the size of large cells. This finding is consistent with previous studies (57). Biological stochasticity (e.g., gene expression fluctuation and asymmetric cell division) and local geometric constraints have been identified to largely influence cell morphology in jammed epithelia. For example, cells that assemble more stress fibers and spread out more have been shown to be stiffer (79-81). Additionally, the local force balance in jammed systems is often achieved by compressing the softer constituents and reducing their size. Alternatively, it is also possible for the converse of this hypothesis to be true, such that cell morphology instead may play a role in regulating cell modulus, although further studies such as micropatterning experiments or inhibition of specific signaling pathways are required to validate these hypotheses.

DISCUSSIONS AND CONCLUSIONS

We reported a microscopy-based cell mechanics characterization platform that allows visualization of supracellular modulus heterogeneities. Our method measures the heterogeneous strain fields in a stretched cell-PDMS bilayer, and converts them into an effective modulus field using an AI-based inference. Using this approach, we measured the effective modulus distribution in MDCK (4.0 \pm 1.5 kPa) and 3T3 (12.2 \pm 3.1 kPa) cell layers. Our measured effective mean modulus values, standard deviations, and correlation lengths are in agreement with previous studies (57, 58, 78). Furthermore, we observed

a mild correlation (Pearson correlation coefficient ~ 0.24) between MDCK cell modulus and area, implying that the cellular stiffness may affect the size and packing of jammed epithelial cells. Collectively, our reported experimental platform and results can provide useful cell mechanics information for improving theoretical models of epithelial jamming (56), collective migration (82), and homeostasis (83), all of which can be influenced by cell stiffness heterogeneity (1).

In our method, we applied a 5% tensile strain to reveal the cell modulus heterogeneity. While such a strain can potentially induce changes in cell behavior, cell stretching experiments are considered relatively non-perturbative (84–86) compared to contact-based cell mechanics measurements (87). In future studies, we aim to reduce the applied strain by improving the imaging resolution and PIV accuracy. In addition, because our stretching experiment operates on the time scale of seconds, we consider the cell layer viscoelasticity, which typically emerges on the time scales of minutes to hours (11, 41, 42, 65– 67, 88, 89), relatively negligible. Furthermore, the timescale of seconds prevents the cell-substrate contacts from rearranging as this typically occurs on the timescale of minutes, and thus ensures the imposed non-slip boundary condition. Overall, our relatively short timescale of stretching primarily probes the elastic response of cell monolayers, which was captured by our FE model. A limitation of our current inference model is that any experimental strain measurement error would lead to AI prediction error, since the FEA strain fields used for training the inference model do not contain any noise. In the future, it would be useful to implement other AI training frameworks including data augmentation and neural network perturbations to improve the robustness of the inference model (90-94).

Similar to other stretching experiments, our method requires growing cells on soft substrates, which can potentially alter cell properties (13, 80, 95). For example, it has been shown that cells exhibit a lower modulus when cultured on a soft substrate (10, 96). While our previous work has shown that jammed epithelial cells with well established intercellular adhesions are not strongly influenced by substrate stiffness (97), it would be useful to conduct further cell mechanics measurements in future experiments. We also acknowledge that the PDMS substrate uniformity plays an important role in our measurement. While it would be ideal to characterize the substrate uniformity of the specific substrate used in experiments, doing so proved to be technically challenging since introducing detectable particles to our substrate for PIV to track significantly altered the local mechanical properties of such a thin, soft substrate. Nevertheless, previous work has demonstrated the mechanical homogeneity of similar elastomeric substrates also used in stretching experiments by calculating the strain resulting from the applied deformation using traction force microscopy (47). The results of such an experiment demonstrate a uniform strain distribution under 10% strain. In addition, other past works have shown that PDMS produces equiaxial and uniform strain fields under

stretching (43, 44), and that both stretched and unstretched PDMS substrate homogeneity has been validated by measuring the modulus of three distinct spatial locations on the substrate, in which all were in statistical agreement with one another (98).

Our effective modulus measurement approach is a useful alternative tool for conducting supracellular-level mechanics studies that require simultaneous access to microscopy. For example, our system can be used for investigating the relationship between cell signaling, gene expression, and mechanics in developing or injured tissues. Moreover, our stretcher is compatible with microscope on-stage incubators, enabling the characterization of the effective modulus field evolution in cell monolayers that undergo phenotypic changes. Such measurements could be utilized to identify mechanical signatures in the development of fibrotic diseases and solid tumors (1).

AUTHOR CONTRIBUTIONS

A.B., Z.G., and N.Y.C.L designed the study. A.B., Z.G., and E.S. performed experiments. B.Z., L.M., and M.KJ. developed the FEA models and generated the numerical data. X.L. and C.H. developed and trained the AI models. A.B., Z.G., E.S., and N.Y.C.L analyzed the experimental data. A.B., Z.G., E.S., and N.Y.C.L wrote the manuscript.

DECLARATION OF INTERESTS

The authors declare no competing interests.

ACKNOWLEDGMENTS

We thank Dorian Luccioni for his assistance with the force measurement development and Lihua Jin for granting us access to essential lab equipment. We also thank Amy Rowat for insightful discussions. This work was funded by the UCLA SPORE in Prostate Cancer Grant (P50 CA092131) and NIH IMSD GM055052. A.B. and N.Y.C.L are grateful for support from NSF CMMI-2029454. L.M. and M.KJ. acknowledge financial support from the National Science Foundation (NSF) under award number CMMI-2053971. M.KJ. is grateful for support from NSF (IIS-1925360, CAREER-2047663, CMMI-2101751).

SUPPLEMENTARY MATERIAL

Supporting material can be found online at XXX.

REFERENCES

- 1. Handorf, A. M., Y. Zhou, M. A. Halanski, and W.-J. Li, 2015. Tissue stiffness dictates development, homeostasis, and disease progression. Organogenesis 11:1–15.
- 2. Stooke-Vaughan, G. A., and O. Campàs, 2018. Physical control of tissue morphogenesis across scales. Current opinion in genetics & development 51:111–119.

- 3. Darby, I. A., B. Laverdet, F. Bonté, and A. Desmoulière, 2014. Fibroblasts and myofibroblasts in wound healing. Clinical, cosmetic and investigational dermatology 7:301.
- 4. Valero, C., E. Javierre, J. M. García-Aznar, and M. J. Gómez-Benito, 2014. A cell-regulatory mechanism involving feedback between contraction and tissue formation guides wound healing progression. PloS one 9:e92774.
- 5. Smith, P. C., C. Martínez, J. Martínez, and C. A. McCulloch, 2019. Role of fibroblast populations in periodontal wound healing and tissue remodeling. Frontiers in physiology 10:270.
- 6. Wiegand, C., and R. White, 2013. Microdeformation in wound healing. Wound Repair and Regeneration 21:793-799.
- 7. Wei, S. C., and J. Yang, 2016. Forcing through tumor metastasis: the interplay between tissue rigidity and epithelial-mesenchymal transition. Trends in cell biology 26:111-120.
- 8. Janshoff, A., 2021. Viscoelasticity of basal plasma membranes and cortices derived from MDCK II cells. Biophysical Reports 1:100024.
- 9. Wells, R. G., 2013. Tissue mechanics and fibrosis. Biochimica et Biophysica Acta (BBA)-Molecular Basis of Disease 1832:884-890.
- 10. Chiang, M. Y., Y. Yangben, N. J. Lin, J. L. Zhong, and L. Yang, 2013. Relationships among cell morphology, intrinsic cell stiffness and cell-substrate interactions. Biomaterials 34:9754-9762.
- 11. Sorba, F., A. Poulin, R. Ischer, H. Shea, and C. Martin-Olmos, 2019. Integrated elastomer-based device for measuring the mechanics of adherent cell monolayers. Lab on a Chip 19:2138-2146.
- 12. Christ, A. F., K. Franze, H. Gautier, P. Moshayedi, J. Fawcett, R. J. Franklin, R. T. Karadottir, and J. Guck, 2010. Mechanical difference between white and gray matter in the rat cerebellum measured by scanning force microscopy. Journal of biomechanics 43:2986–2992.
- 13. Discher, D. E., P. Janmey, and Y.-l. Wang, 2005. Tissue cells feel and respond to the stiffness of their substrate. Science 310:1139-1143.
- 14. Franze, K., J. Gerdelmann, M. Weick, T. Betz, S. Pawlizak, M. Lakadamyali, J. Bayer, K. Rillich, M. Gögler, Y.-B. Lu, et al., 2009. Neurite branch retraction is caused by a threshold-dependent mechanical impact. Biophysical journal 97:1883-1890.

- 15. Thompson, A. J., E. K. Pillai, I. B. Dimov, S. K. Foster, C. E. Holt, and K. Franze, 2019. Rapid changes in tissue mechanics regulate cell behaviour in the developing embryonic brain. Elife 8:e39356.
- 16. Polio, S. R., S. E. Stasiak, R. R. Jamieson, J. L. Balestrini, R. Krishnan, and H. Parameswaran, 2019. Extracellular matrix stiffness regulates human airway smooth muscle contraction by altering the cell-cell coupling. Scientific reports 9:1-12.
- 17. de Bruyn, J. R., G. R. van den Brink, J. Steenkamer, C. J. Buskens, W. A. Bemelman, S. Meisner, V. Muncan, A. A. Te Velde, G. R. D'Haens, and M. E. Wildenberg, 2018. Fibrostenotic phenotype of myofibroblasts in Crohn's disease is dependent on tissue stiffness and reversed by LOX inhibition. Journal of Crohn's and Colitis 12:849-859.
- 18. Gavara, N., 2017. A beginner's guide to atomic force microscopy probing for cell mechanics. Microscopy research and technique 80:75-84.
- 19. Remmerbach, T. W., F. Wottawah, J. Dietrich, B. Lincoln, C. Wittekind, and J. Guck, 2009. Oral cancer diagnosis by mechanical phenotyping. Cancer research 69:1728– 1732.
- 20. Lange, J. R., and B. Fabry, 2013. Cell and tissue mechanics in cell migration. Experimental cell research 319:2418-2423.
- 21. Wang, N., I. M. Tolic-Nørrelykke, J. Chen, S. M. Mijailovich, J. P. Butler, J. J. Fredberg, and D. Stamenovic, 2002. Cell prestress. I. Stiffness and prestress are closely associated in adherent contractile cells. American Journal of Physiology-Cell Physiology 282:C606–C616.
- 22. Amoyel, M., and E. A. Bach, 2014. Cell competition: how to eliminate your neighbours. Development 141:988-1000.
- 23. Di Gregorio, A., S. Bowling, and T. A. Rodriguez, 2016. Cell competition and its role in the regulation of cell fitness from development to cancer. Developmental cell 38:621-634.
- 24. Powell, K., 2019. These secret battles between your body's cells might just save your life. Nature 574:310-313.
- 25. Murphy, R. J., P. R. Buenzli, R. E. Baker, and M. J. Simpson, 2020. Mechanical cell competition in heterogeneous epithelial tissues. Bulletin of Mathematical Biology 82:1–27.
- 26. Lee, L. M., and A. P. Liu, 2014. The application of micropipette aspiration in molecular mechanics of single cells. Journal of nanotechnology in engineering and medicine 5.

- 27. Guevorkian, K., and J.-L. Maître, 2017. Micropipette aspiration: A unique tool for exploring cell and tissue mechanics in vivo. In Methods in cell biology, Elsevier, volume 139, 187-201.
- 28. Mierke, C. T. The micropipette aspiration technique.
- 29. You, H. X., and L. Yu, 1999. Atomic force microscopy imaging of living cells: progress, problems and prospects. Methods in cell science 21:1–17.
- 30. Müller, D. J., and Y. F. Dufrêne, 2011. Atomic force microscopy: a nanoscopic window on the cell surface. *Trends in cell biology* 21:461–469.
- 31. Hoh, J. H., and C.-A. Schoenenberger, 1994. Surface morphology and mechanical properties of MDCK monolayers by atomic force microscopy. Journal of cell science 107:1105-1114.
- 32. Zhang, Y., F. Wei, Y.-C. Poh, Q. Jia, J. Chen, J. Chen, J. Luo, W. Yao, W. Zhou, W. Huang, et al., 2017. Interfacing 3D magnetic twisting cytometry with confocal fluorescence microscopy to image force responses in living cells. *Nature protocols* 12:1437–1450.
- 33. Serwane, F., A. Mongera, P. Rowghanian, D. A. Kealhofer, A. A. Lucio, Z. M. Hockenbery, and O. Campas, 2017. In vivo quantification of spatially varying mechanical properties in developing tissues. Nature methods 14:181– 186.
- 34. Gómez-González, M., E. Latorre, M. Arroyo, and X. Trepat, 2020. Measuring mechanical stress in living tissues. Nature Reviews Physics 2:300–317.
- 35. Kong, W., O. Loison, P. Chavadimane Shivakumar, E. H. Chan, M. Saadaoui, C. Collinet, P.-F. Lenne, and R. Clément, 2019. Experimental validation of force inference in epithelia from cell to tissue scale. Scientific reports 9:1-12.
- 36. Maître, J.-L., H. Turlier, R. Illukkumbura, B. Eismann, R. Niwayama, F. Nédélec, and T. Hiiragi, 2016. Asymmetric division of contractile domains couples cell positioning and fate specification. *Nature* 536:344–348.
- 37. Maître, J.-L., R. Niwayama, H. Turlier, F. Nédélec, and T. Hiiragi, 2015. Pulsatile cell-autonomous contractility drives compaction in the mouse embryo. Nature cell biology 17:849-855.
- 38. Thevenaz, P., U. E. Ruttimann, and M. Unser, 1998. A pyramid approach to subpixel registration based on intensity. IEEE transactions on image processing 7:27-41.

- 39. Thielicke, W., and R. Sonntag, 2021. Particle Image Velocimetry for MATLAB: Accuracy and enhanced algorithms in PIVlab. Journal of Open Research Software 9.
- 40. Liu, Y., K. Mollaeian, and J. Ren, 2019. Finite element modeling of living cells for AFM indentation-based biomechanical characterization. Micron 116:108–115.
- 41. Schulze, K., S. Zehnder, J. Urueña, T. Bhattacharjee, W. Sawyer, and T. Angelini, 2017. Elastic modulus and hydraulic permeability of MDCK monolayers. Journal of Biomechanics 53:210-213.
- 42. Harris, A. R., L. Peter, J. Bellis, B. Baum, A. J. Kabla, and G. T. Charras, 2012. Characterizing the mechanics of cultured cell monolayers. Proceedings of the National Academy of Sciences 109:16449-16454.
- 43. Kreutzer, J., L. Ikonen, J. Hirvonen, M. Pekkanen-Mattila, K. Aalto-Setälä, and P. Kallio, 2014. Pneumatic cell stretching system for cardiac differentiation and culture. Medical engineering & physics 36:496-501.
- 44. Bartalena, G., R. Grieder, R. I. Sharma, T. Zambelli, R. Muff, and J. G. Snedeker, 2011. A novel method for assessing adherent single-cell stiffness in tension: design and testing of a substrate-based live cell functional imaging device. Biomedical microdevices 13:291–301.
- 45. Gong, Z., S. E. Szczesny, S. R. Caliari, E. E. Charrier, O. Chaudhuri, X. Cao, Y. Lin, R. L. Mauck, P. A. Janmey, J. A. Burdick, et al., 2018. Matching material and cellular timescales maximizes cell spreading on viscoelastic substrates. Proceedings of the National Academy of Sciences 115:E2686-E2695.
- 46. Ghosh, S., V. C. Cuevas, B. Seelbinder, and C. P. Neu, 2021. Image-Based Elastography of Heterochromatin and Euchromatin Domains in the Deforming Cell Nucleus. Small 17:2006109.
- 47. Seelbinder, B., A. K. Scott, I. Nelson, S. E. Schneider, K. Calahan, and C. P. Neu, 2020. TENSCell: imaging of stretch-activated cells reveals divergent nuclear behavior and tension. Biophysical journal 118:2627–2640.
- 48. Friedrich, O., A.-L. Merten, D. Schneidereit, Y. Guo, S. Schürmann, and B. Martinac, 2019. Stretch in focus: 2D inplane cell stretch systems for studies of cardiac mechano-signaling. Frontiers in Bioengineering and Biotechnology 7:55.
- 49. Boulogne, F., Y. L. Kong, J. K. Nunes, and H. A. Stone, 2016. Effect of the polydispersity of a colloidal drop on drying induced stress as measured by the buckling of a floating sheet. Physical review letters 116:238001.

- 50. Addae-Mensah, K. A., R. S. Reiserer, and J. P. Wikswo, 2007. Poly (vinyl alcohol) as a structure release layer for the microfabrication of polymer composite structures. Journal of Micromechanics and Microengineering 17:N41.
- 51. Plotnikov, S. V., B. Sabass, U. S. Schwarz, and C. M. Waterman, 2014. High-resolution traction force microscopy. In Methods in cell biology, Elsevier, volume 123, 367– 394.
- 52. Sabass, B., M. L. Gardel, C. M. Waterman, and U. S. Schwarz, 2008. High resolution traction force microscopy based on experimental and computational advances. Biophysical journal 94:207-220.
- 53. Vincent, R., E. Bazellières, C. Pérez-González, M. Uroz, X. Serra-Picamal, and X. Trepat, 2015. Active tensile modulus of an epithelial monolayer. Physical review letters 115:248103.
- 54. Serra-Picamal, X., V. Conte, R. Vincent, E. Anon, D. T. Tambe, E. Bazellieres, J. P. Butler, J. J. Fredberg, and X. Trepat, 2012. Mechanical waves during tissue expansion. Nature Physics 8:628-634.
- 55. Nobach, H., and E. Bodenschatz, 2009. Limitations of accuracy in PIV due to individual variations of particle image intensities. Experiments in fluids 47:27–38.
- 56. Fujii, Y., Y. Ochi, M. Tuchiya, M. Kajita, Y. Fujita, Y. Ishimoto, and T. Okajima, 2019. Spontaneous spatial correlation of elastic modulus in jammed epithelial monolayers observed by AFM. Biophysical journal 116:1152–1158.
- 57. Nehls, S., H. Nöding, S. Karsch, F. Ries, and A. Janshoff, 2019. Stiffness of MDCK II cells depends on confluency and cell size. Biophysical journal 116:2204–2211.
- 58. Pietuch, A., B. R. Brückner, D. Schneider, M. Tarantola, C. Rosman, C. Sönnichsen, and A. Janshoff, 2015. Mechanical properties of MDCK II cells exposed to gold nanorods. Beilstein Journal of Nanotechnology 6:223– 231.
- 59. Ronneberger, O., P. Fischer, and T. Brox, 2015. U-net: Convolutional networks for biomedical image segmentation. In International Conference on Medical image computing and computer-assisted intervention. Springer, 234-241.
- 60. Ounkomol, C., S. Seshamani, M. M. Maleckar, F. Collman, and G. R. Johnson, 2018. Label-free prediction of three-dimensional fluorescence images from transmittedlight microscopy. Nature methods 15:917–920.
- 61. Isola, P., J.-Y. Zhu, T. Zhou, and A. A. Efros, 2017. Image-to-image translation with conditional adversarial networks. In Proceedings of the IEEE conference on computer vision and pattern recognition. 1125–1134.

- 62. Elitas, M., and E. Sengul, 2021. Optimization of U-Net: convolutional networks for U87 human glioblastoma cell line segmentation. In Emerging Topics in Artificial Intelligence (ETAI) 2021. International Society for Optics and Photonics, volume 11804, 118041G.
- 63. Zhang, Y., J.-H. Chen, K.-T. Chang, V. Y. Park, M. J. Kim, S. Chan, P. Chang, D. Chow, A. Luk, T. Kwong, et al., 2019. Automatic breast and fibroglandular tissue segmentation in breast MRI using deep learning by a fullyconvolutional residual neural network U-net. Academic radiology 26:1526-1535.
- 64. Hashemi-Beni, L., and A. Gebrehiwot, 2020. Deep learning for remote sensing image classification for agriculture applications. The International Archives of Photogrammetry, Remote Sensing and Spatial Information Sciences 51-54.
- 65. Khalilgharibi, N., J. Fouchard, N. Asadipour, R. Barrientos, M. Duda, A. Bonfanti, A. Yonis, A. Harris, P. Mosaffa, Y. Fujita, et al., 2019. Stress relaxation in epithelial monolayers is controlled by the actomyosin cortex. Nature physics 15:839-847.
- 66. Pajic-Lijakovic, I., and M. Milivojevic, 2019. Long-time viscoelasticity of multicellular surfaces caused by collective cell migration-multi-scale modeling considerations. In Seminars in Cell & Developmental Biology. Elsevier, volume 93, 87-96.
- 67. Thoumine, O., and A. Ott, 1997. Time scale dependent viscoelastic and contractile regimes in fibroblasts probed by microplate manipulation. Journal of cell science 110:2109-2116.
- 68. Liu, G., 2019. FEA-AI and AI-AI: Two-way deepnets for real-time computations for both forward and inverse mechanics problems. International Journal of Computational Methods 16:1950045.
- 69. Tallman, J. A., M. Osusky, N. Magina, and E. Sewall, 2019. An assessment of machine learning techniques for predicting turbine airfoil component temperatures, using FEA simulations for training data. *In* Turbo Expo: Power for Land, Sea, and Air. American Society of Mechanical Engineers, volume 58646, V05AT20A002.
- 70. Cho, K.-H., S.-M. Choo, S. Jung, J.-R. Kim, H.-S. Choi, and J. Kim, 2007. Reverse engineering of gene regulatory networks. IET Systems Biology 1:149-163.
- 71. Varady, T., R. R. Martin, and J. Cox, 1997. Reverse engineering of geometric models—an introduction. Computeraided design 29:255-268.
- 72. Martin, R., I. Stroud, and A. Marshall, 1997. Data reduction for reverse engineering. RECCAD, Deliverable Document 1 COPERNICUS project, No 1068 111.

- 73. Bertero, M., R. Jost, et al., 1980. Inverse scattering problems in optics, volume 20. Springer Verlag.
- 74. Guimarães, C. F., L. Gasperini, A. P. Marques, and R. L. Reis, 2020. The stiffness of living tissues and its implications for tissue engineering. Nature Reviews *Materials* 5:351–370.
- 75. Luo, Q., D. Kuang, B. Zhang, and G. Song, 2016. Cell stiffness determined by atomic force microscopy and its correlation with cell motility. Biochimica et Biophysica Acta (BBA)-General Subjects 1860:1953-1960.
- 76. Michaelson, J., H. Choi, P. So, and H. Huang, 2012. Mechanical Properties of Primary and Immortal Fibroblasts in Cell Bi-Layers. In Summer Bioengineering Conference. American Society of Mechanical Engineers, volume 44809, 685-686.
- 77. Hutter, J., J. Chen, W. Wan, S. Uniyal, M. Leabu, and B. Chan, 2005. Atomic force microscopy investigation of the dependence of cellular elastic moduli on glutaraldehyde fixation. Journal of microscopy 219:61-68.
- 78. Rotsch, C., K. Jacobson, and M. Radmacher, 1999. Dimensional and mechanical dynamics of active and stable edges in motile fibroblasts investigated by using atomic force microscopy. Proceedings of the National Academy of Sciences 96:921-926.
- 79. Vichare, S., M. M. Inamdar, and S. Sen, 2012. Influence of cell spreading and contractility on stiffness measurements using AFM. Soft Matter 8:10464-10471.
- 80. Tee, S.-Y., J. Fu, C. S. Chen, and P. A. Janmey, 2011. Cell shape and substrate rigidity both regulate cell stiffness. Biophysical journal 100:L25–L27.
- 81. Stroka, K. M., and H. Aranda-Espinoza, 2011. Effects of morphology vs. cell-cell interactions on endothelial cell stiffness. Cellular and molecular bioengineering 4:9–27.
- 82. Ebata, H., and S. Kidoaki, 2021. Avoiding tensional equilibrium in cells migrating on a matrix with cell-scale stiffness-heterogeneity. Biomaterials 274:120860.
- 83. Cox, T. R., and J. T. Erler, 2011. Remodeling and homeostasis of the extracellular matrix: implications for fibrotic diseases and cancer. Disease models & mechanisms 4:165-178.
- 84. Cui, Y., F. M. Hameed, B. Yang, K. Lee, C. Q. Pan, S. Park, and M. Sheetz, 2015. Cyclic stretching of soft substrates induces spreading and growth. Nature communications 6:1-8.
- 85. Kamble, H., M. J. Barton, M. Jun, S. Park, and N.-T. Nguyen, 2016. Cell stretching devices as research tools: engineering and biological considerations. Lab on a Chip 16:3193-3203.

- 86. Wang, J. H.-C., G. Yang, and Z. Li, 2005. Controlling cell responses to cyclic mechanical stretching. Annals of biomedical engineering 33:337–342.
- 87. Schaus, S. S., and E. R. Henderson, 1997. Cell viability and probe-cell membrane interactions of XR1 glial cells imaged by atomic force microscopy. Biophysical journal 73:1205-1214.
- 88. Esfahani, A. M., J. Rosenbohm, B. T. Safa, N. V. Lavrik, G. Minnick, Q. Zhou, F. Kong, X. Jin, E. Kim, Y. Liu, et al., 2021. Characterization of the strain-ratedependent mechanical response of single cell-cell junctions. Proceedings of the National Academy of Sciences 118:e2019347118.
- 89. Kubitschke, H., J. Schnauß, K. D. Nnetu, E. Warmt, R. Stange, and J. Kaes, 2017. Actin and microtubule networks contribute differently to cell response for small and large strains. New Journal of Physics 19:093003.
- 90. Wang, Y., X. Pan, S. Song, H. Zhang, G. Huang, and C. Wu, 2019. Implicit semantic data augmentation for deep networks. Advances in Neural Information Processing Systems 32.
- 91. Mikołajczyk, A., and M. Grochowski, 2018. Data augmentation for improving deep learning in image classification problem. In 2018 international interdisciplinary PhD workshop (IIPhDW). IEEE, 117-122.
- 92. Kong, L., C. Lian, D. Huang, Y. Hu, Q. Zhou, et al., 2021. Breaking the dilemma of medical image-to-image translation. Advances in Neural Information Processing Systems 34:1964-1978.
- 93. Mustafa, A., and R. K. Mantiuk, 2020. Transformation consistency regularization-a semi-supervised paradigm for image-to-image translation. *In* European Conference on Computer Vision. Springer, 599-615.
- 94. Romero, A., P. Arbelaez, L. Van Gool, and R. Timofte, 2019. SMIT: Stochastic Multi-Label Image-to-Image Translation. In Proceedings of the IEEE/CVF International Conference on Computer Vision (ICCV) Workshops.
- 95. Yeung, T., P. C. Georges, L. A. Flanagan, B. Marg, M. Ortiz, M. Funaki, N. Zahir, W. Ming, V. Weaver, and P. A. Janmey, 2005. Effects of substrate stiffness on cell morphology, cytoskeletal structure, and adhesion. Cell motility and the cytoskeleton 60:24-34.
- 96. Jalali, S., M. Tafazzoli-Shadpour, N. Haghighipour, R. Omidvar, and F. Safshekan, 2015. Regulation of endothelial cell adherence and elastic modulus by substrate stiffness. Cell communication & adhesion 22:79-89.

- 97. Choi, D., Z. Gonzalez, S. Y. Ho, A. Bermudez, and N. Y. Lin, 2022. Cell-cell adhesion impacts epithelia response to substrate stiffness: Morphology and gene expression. Biophysical Journal 121:336-346.
- 98. Boulter, E., F. S. Tissot, J. Dilly, S. Pisano, and C. C. Féral, 2020. Cyclic uniaxial mechanical stretching of cells using a LEGO® parts-based mechanical stretcher system. Journal of cell science 133:jcs234666.

